Nondegenerate Kuznetsov-Ma solitons of Manakov equations and their physical spectra

Wen-Juan Che,[1] Shao-Chun Chen,[1] Chong Liu,[1,2,3,4,*] Li-Chen Zhao,[1,3,4,†] and Nail Akhmediev [2,‡]

[1]*School of Physics, Northwest University, Xi'an 710127, China*
[2]*Optical Sciences Group, Department of Fundamental and Theoretical Physics, Research School of Physics,*
Australian National University, Canberra, Australian Capital Territory 2600, Australia
[3]*Shaanxi Key Laboratory for Theoretical Physics Frontiers, Xi'an 710127, China*
[4]*NSFC-SPTP Peng Huanwu Center for Fundamental Theory, Xi'an 710127, China*

We study the dynamics of Kuznetsov-Ma solitons (KMSs) in the framework of vector nonlinear Schrödinger (Manakov) equations. An exact multiparameter family of solutions for such KMSs is derived. This family of solutions includes the known results as well as the previously unknown solutions in the form of nondegenerate KMSs. We present the existence diagram of such KMSs that follows from the exact solutions. These nondegenerate KMSs are formed by nonlinear superposition of two fundamental KMSs that have the same propagation period but different eigenvalues. We present the amplitude profiles of solutions, their exact physical spectra, and their link to ordinary vector solitons and offer easy ways for their excitation using numerical simulations.

I. INTRODUCTION

Oscillating localized structures in a wide variety of conservative and dissipative systems known as breathers have attracted considerable interest in recent decades [1–7]. They are known in optics [8], hydrodynamics [9], Bose-Einstein condensates [6], micromechanical arrays [10], and cavity optomechanics [11]. Breathers play a crucial role in understanding various nonlinear coherent phenomena, including modulation instability [12,13], Fermi-Pasta-Ulam recurrence [14], rogue wave events [15], supercontinuum generation [16], and even turbulence [17].

In conservative integrable systems governed by the scalar nonlinear Schrödinger equation (NLSE), fundamental (first-order) breathers can be presented in the form of a multiparameter family of solutions that are periodic both in time and in space [18,19]. Comprehensive analysis of all physical effects described by this family is difficult due to the presence of free parameters in the solution and a large variety of possibilities [19]. Subdividing the whole family into particular cases simplifies the task. Among the particular cases of this general family we can select the class of breathers on a plane-wave background that are periodic in the transverse direction [18,19]. These are known as Akhmediev breathers. Another class of solutions is solitons on a constant background. Due to the beating between the soliton and the background, these solitons are periodic in the propagation direction. These are known as Kuznetsov-Ma solitons (KMSs) [20,21]. As these solitons are periodic, sometimes they are also dubbed Kuznetsov-Ma breathers. Periods in each of these subfamilies of solutions are variable parameters.

When the period in either space or time becomes large, the common limit of each of these subfamilies is the Peregrine soliton. It has an infinite breathing period both in time and in space, thus describing an isolated event such as a rogue wave. Recent results [22,23] reveal the universal role that the Peregrine soliton plays in complex dynamics of multisoliton evolution.

The KMS is oscillating due to the coherent interaction with a constant background [24,25]. When the amplitude of the background tends to zero, the period of oscillations increases and in the zero limit the KMS turns into an ordinary bright soliton [24]. The periodic evolution in propagation of the KMS has been observed experimentally both in fiber optics [26] and in hydrodynamics [27]. Kuznetsov-Ma solitons should not be confused with pulsating solitons in dissipative optical systems [28,29], where the physical reason for soliton oscillations is different. Oscillations can also appear as a result of beating between several solitons in higher-order solutions [30–32].

The single NLSE describes the nonlinear dynamics of a scalar wave field. On the other hand, the nonlinear interaction of two or more coupled wave components is common in physics. Such interaction is important in optical fibers [33], in Bose-Einstein condensates [34], and in multidirectional wave dynamics in the open ocean known as crossing seas [35]. The mathematical model that describes the interaction of two wave components is commonly based on Manakov equations [36–49]. The interaction between the two wave components makes the wave dynamics more complex. One example is the presence of unusual dark and four-petal structures in such systems [46,47]. Another example is dark breathers with an infinite period (dark rogue waves). The latter have been observed experimentally in fiber optics [48,49]. Even when considering common soliton solutions, Manakov equations admit qualitatively new types of formations such as nondegenerate solitons [50–53].

*chongliu@nwu.edu.cn
†zhaolichen3@nwu.edu.cn
‡Nail.Akhmediev@anu.edu.au

In this work we present theoretical and numerical studies of KMS dynamics in the model governed by the Manakov equations. We derive a family of multiparameter vector KMS solutions. We show that this family contains a nondegenerate family that has no analogs in the case of scalar KMSs. We analyze their amplitude profiles and their physical spectra and using numerical simulations suggest an easy way of excitation of these solutions. Just as in the scalar case, solitons are the limiting cases of KMSs in the vector model as well. However, finding the link between the KMSs and ordinary solitons in the vector case has been elusive. Here we fill this gap in the existing knowledge and find the limit of vector KMSs when they are converted to nondegenerate vector solitons.

II. MANAKOV EQUATIONS, THEIR KMS SOLUTIONS, AND THE CORRESPONDING SYMMETRIES

The Manakov equations in dimensionless form are given by [54]

$$
\begin{aligned}
i\frac{\partial \psi^{(1)}}{\partial t} + \frac{1}{2}\frac{\partial^2 \psi^{(1)}}{\partial x^2} + (|\psi^{(1)}|^2 + |\psi^{(2)}|^2)\psi^{(1)} = 0, \\
i\frac{\partial \psi^{(2)}}{\partial t} + \frac{1}{2}\frac{\partial^2 \psi^{(2)}}{\partial x^2} + (|\psi^{(1)}|^2 + |\psi^{(2)}|^2)\psi^{(2)} = 0,
\end{aligned}
\tag{1}
$$

where $\psi^{(1)}(t,x)$ and $\psi^{(2)}(t,x)$ are the two nonlinearly coupled components of the vector wave field. The physical meaning of the variables x and t depends on a particular physical problem of interest. In optics, t is commonly a normalized distance along the fiber, while x is the normalized time in a frame moving with the group velocity [33]. In the case of Bose-Einstein condensates, t is time, while x is the spatial coordinate [34]. The choice of signs for the dispersion and nonlinear terms in Eqs. (1) corresponds (in optics) to the self-focusing effect and anomalous dispersion regime.

A fundamental (first-order) solution for vector KMSs [i.e., $\psi_1^{(j)}(t,x)$] in compact form obtained using a Darboux transformation scheme is given by

$$
\psi_1^{(j)}(t,x) = \rho_j \psi_0^{(j)}(t,x)\psi_{km}^{(j)}(t,x),
\tag{2}
$$

where $\psi_0^{(j)}$ is the background vector plane wave

$$
\psi_0^{(j)} = a_j \exp\left\{i\left[\beta_j x + \left(a_1^2 + a_2^2 - \tfrac{1}{2}\beta_j^2\right)t\right]\right\},
\tag{3}
$$

with a_j the two real amplitudes and β_j the wave numbers of the background waves, and

$$
\rho^{(j)} = \frac{\tilde{\chi}^* + \beta_j}{\tilde{\chi} + \beta_j}\sqrt{\frac{(\chi^* + \beta_j)(\tilde{\chi}^* + \beta_j)}{(\chi + \beta_j)(\tilde{\chi} + \beta_j)}},
\tag{4}
$$

$$
\psi_{km}^{(j)} = \frac{\varpi \cosh(\Gamma + i\delta_j) + \cos(\Omega + i\gamma_j)}{\varpi \cosh\Gamma + \cos\Omega},
\tag{5}
$$

where

$$
\Gamma = \alpha(x + \chi_r t) + \frac{1}{2}\ln\left(\frac{\alpha + \chi_i}{\chi_i}\right),
\tag{6}
$$

$$
\Omega = \Omega t = \alpha\left(\frac{\alpha}{2} + \chi_i\right)t,
\tag{7}
$$

and

$$
\tilde{\chi} = \chi + i\alpha,
\tag{8}
$$

where α is a real parameter. Without loss of generality, we set $\alpha \geqslant 0$. Subscripts r and i in (6) and (7) denote the real and imaginary parts of the complex parameter χ, respectively. The latter is the eigenvalue of the Manakov system (1), which obeys the relation

$$
1 + \sum_{j=1}^{2}\frac{a_j^2}{(\chi - \beta_j)(\tilde{\chi} - \beta_j)} = 0.
\tag{9}
$$

The relation between the eigenvalue and the spectral parameter of the associated Lax pair is given by

$$
\lambda = \chi - \sum_{j=1}^{2}\frac{a_j^2}{\chi + \beta_j}.
\tag{10}
$$

The other parameters in Eq. (5) are

$$
\delta_j = \arg[(\chi^* + \beta_j)(\chi + i\alpha + \beta_j)],
\tag{11}
$$

$$
\gamma_j = -\frac{1}{2}\ln\left[\frac{(\chi^* - i\alpha + \beta_j)(\chi + i\alpha + \beta_j)}{(\chi^* + \beta_j)(\chi + \beta_j)}\right],
\tag{12}
$$

$$
\varpi = \frac{\alpha + 2\chi_i}{2\alpha + 2\chi_i}\sqrt{\frac{\alpha + \chi_i}{\chi_i}}.
\tag{13}
$$

From here, one can readily confirm that $|\rho^{(j)}| = 1$. The solution (2) depends on the background parameters a_j and β_j and the real parameter α.

From a physical perspective, an important parameter is the relative wave number $\beta_1 - \beta_2$, since it cannot be eliminated through Galilean transformation. Indeed, when $\beta_1 = \beta_2$, for any eigenvalue given by Eq. (9), $\psi_1^{(1)}$ is merely proportional to $\psi_1^{(2)}$, i.e., $\psi_1^{(1)}/\psi_1^{(2)} = a_1/a_2$. The solution (2) contains the trivial vector generalization of the scalar KMS solution which has been found in [55]. Our solution is far from being a simple rotation on a $(\psi^{(1)}, \psi^{(2)})$ plane. As it will be shown below, it has nontrivial properties of vector KMSs once $\beta_1 \neq \beta_2$. Without loss of generality, we can set $\beta_1 = -\beta_2 = \beta \neq 0$.

Physically, the solution (2) describes solitons located on top of plane-wave backgrounds (3). Such solitons are localized in x (the width is $\sim 1/\alpha$) and they propagate along t with the group velocity $V_g = -\chi_r$. Due to the beating with the background, the amplitude of the soliton oscillates periodically along the t axis. In the limiting case of the infinite period, which implies $\alpha \to 0$, the solution (2) is transformed into the vector rogue wave.

The solution (2) has two symmetries. The first one is the symmetry of the solution (2) relative to the sign change of β and simultaneous exchange of the wave component. When the background amplitudes are equal $a_1 = a_2 = a$, this means

$$
\psi_1^{(1)}(\beta) = \psi_1^{(2)}(-\beta), \quad \beta \neq 0.
\tag{14}
$$

The second symmetry of the vector solution is more complicated. Namely, if $\chi_i \Rightarrow -\chi_i - \alpha$, then

$$
\psi^{(j)}\{(x,t);\chi_i\} = \psi^{(j)}\{(x+\Delta x, t+\Delta t); -\chi_i - \alpha\}e^{(-i\mathbf{r}_j)},
\tag{15}
$$

where $x' = x + \Delta x$ and $t' = t + \Delta t$, with Δx and Δt fixed constant shifts along the x and t axes, respectively, and $\mathbf{r}_j$ are

constant phases. The shifts are given by

$$\Delta x = -\frac{1}{\alpha}\left(\frac{4\pi \chi_r}{\alpha + 2\chi_i} + \ln\left[\frac{\alpha + \chi_i}{\chi_i}\right]\right), \qquad (16)$$

$$\Delta t = \frac{4\pi}{\alpha^2 + 2\alpha\chi_i}, \qquad \mathbf{r}_j = 2\arg(\rho^{(j)}). \qquad (17)$$

The symmetry (15) means that the vector KMSs have periodic amplitude profiles:

$$\left|\psi_1^{(j)}[(x, t); \chi_i]\right| = \left|\psi_1^{(j)}[(x', t'); -\chi_i - \alpha]\right|. \qquad (18)$$

The symmetries (14) and (15) serve as a basis for revealing the richness of KMS properties found below.

The form of the KMS solution (2) has an important advantage. It can be analyzed using the Hessian matrix theory [46,47]. In order to do that, we introduce the derivatives $|\psi_{km}^{(j)}|_{\mathbf{\Gamma}}$ and $|\psi_{km}^{(j)}|_{\mathbf{\Omega}}$. Then the zero derivatives $|\psi_{km}^{(j)}|_{\mathbf{\Gamma}} = 0$ and $|\psi_{km}^{(j)}|_{\mathbf{\Omega}} = 0$ define the special points in each cell of t-periodic pattern of the KMS. One of them (at the center) is given by $(\mathbf{\Omega}, \mathbf{\Gamma}) = (0, \pi)$. The type of these points can be revealed using the Hessian matrix

$$H^{(j)} = \begin{pmatrix} |\psi_{km}^{(j)}|_{\mathbf{\Gamma}\mathbf{\Gamma}} & |\psi_{km}^{(j)}|_{\mathbf{\Gamma}\mathbf{\Omega}} \\ |\psi_{km}^{(j)}|_{\mathbf{\Omega}\mathbf{\Gamma}} & |\psi_{km}^{(j)}|_{\mathbf{\Omega}\mathbf{\Omega}} \end{pmatrix}. \qquad (19)$$

Three distinctive cases which correspond to three different types of KMS can be identified from this analysis. We call them bright, four-petal, and dark solitons. They are shown in Fig. 1.

(a) When $\det(H^{(j)}) > 0$ and $|\psi_{km}^{(j)}|_{\mathbf{\Gamma}\mathbf{\Gamma}}^2 < 0$, the Hessian is a negative-definite matrix. This implies that the special point is a maximum. The two components $\psi_1^{(j)}(t, x)$ of the solution in this case have classical bright structure. This case is shown in Fig. 1(a). The point of maximal compression in the periodic soliton evolution has a high bump and two small dips on each side of it.

(b) When $\det(H^{(j)}) < 0$, the Hessian is an indefinite matrix. The center of each period in this case is a saddle point. The two components of the soliton profile are shown in Fig. 1(b). Here the pattern of the second component $\psi_1^{(2)}(t, x)$ can be called a four-petal structure. Namely, each period has two bumps and two dips symmetrically located around the center.

(c) When $\det(H^{(j)}) > 0$ and $|\psi_{km}^{(j)}|_{\mathbf{\Gamma}\mathbf{\Gamma}}^2 > 0$, the Hessian is a positive-definite matrix. In this case, the second component $\psi_1^{(2)}(t, x)$ is a periodic repetition of dark structures as can be seen in Fig. 1(c). The central point in each cell is a minimum. It is surrounded by two small bumps on the sides.

III. EXACT ANALYTIC SPECTRA OF THE KMS

Commonly measured characteristics of solitons and breathers are their physical spectra. They are often measured experimentally in optics and hydrodynamics. One example is the Akhmediev breathers (ABs). The AB spectra can be calculated in analytic form [12]. These spectra are discrete and have an infinite number of sidebands decaying in a geometric progression [12]. Recent experimental observation of more than ten spectral sidebands in an optical fiber [56] confirmed the theoretical predictions. In contrast to the ABs, which are periodic in the transverse variable and therefore have discrete
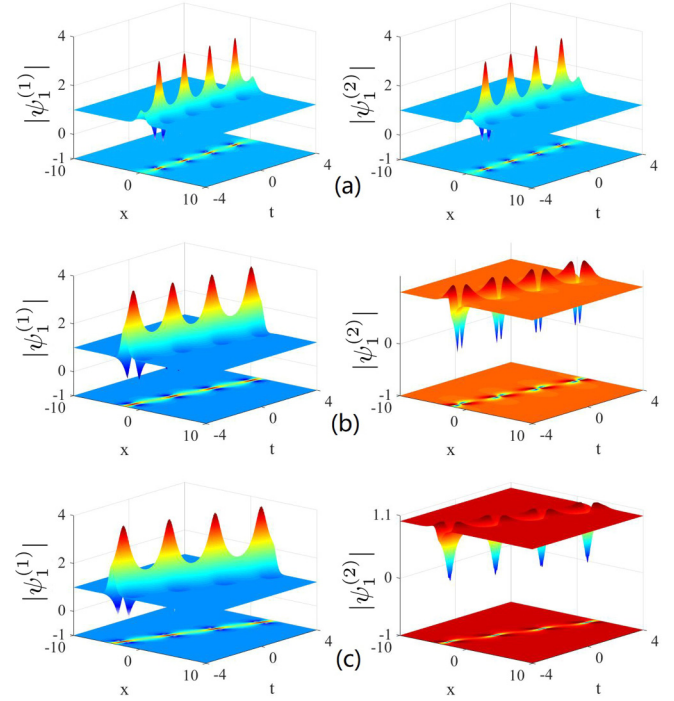

FIG. 1. Amplitude profiles of the two components of the vector KMS $|\psi_1^{(j)}(t, x)|$ for three different relative background wave numbers producing qualitatively different wave patterns: (a) $\beta = 0.3$, (b) $\beta = 0.6$, and (c) $\beta = 1$. The other parameters are $a = 1$ and $\alpha = 2$. All variables in this plot and the plots below are dimensionless in accordance with the choice of units in Eq. (1) and in the following equations

spectra, the spectra of the KMS are continuous. They can be calculated using the Fourier transform

$$A_\omega^{(j)}(\omega, t) = \frac{1}{2\pi}\int_{-\infty}^{\infty}\psi^{(j)}(t, x)e^{-i\omega x}dx. \qquad (20)$$

However, finding the exact analytic KMS spectra is far from being a trivial task due to the symmetry breaking of the Manakov system. In our previous works [13,47], we gave some examples of asymmetric discrete spectra in analytic form. Here we present calculations of the exact analytic continuous spectra of the vector KMS (2).

Let us first rewrite the solution (2) in the form

$$\psi^{(j)} = \psi_0^{(j)}\rho^{(j)}[1 + \psi_a(x, t)], \qquad (21)$$

where the new function $\psi_a(x, t)$ is given by

$$\psi_a(x, t) = \frac{\mathcal{B}_1(t) + \mathcal{B}_2(t)e^{\alpha x} + \mathcal{B}_3(t)e^{-\alpha x}}{\mathcal{D}_1(t) + \mathcal{D}_2(t)e^{\alpha x} + \mathcal{D}_3(t)e^{-\alpha x}}, \qquad (22)$$

with

$$\mathcal{B}_1(t) = e^{\gamma_j - i\mathbf{\Omega}} + e^{-\gamma_j + i\mathbf{\Omega}} - e^{i\mathbf{\Omega}} - e^{-i\mathbf{\Omega}},$$

$$\mathcal{B}_2(t) = \varpi(e^{\mathbf{\Gamma} - \alpha x} - e^{\mathbf{\Gamma} - \alpha x + i\delta_j}),$$

$$\mathcal{B}_3(t) = \varpi(e^{-(\mathbf{\Gamma} - \alpha x)} - e^{-(\mathbf{\Gamma} - \alpha x) + i\delta_j}),$$

$$\mathcal{D}_1(t) = e^{i\mathbf{\Omega}} + e^{-i\mathbf{\Omega}},$$

$$\mathcal{D}_2(t) = \varpi e^{\mathbf{\Gamma} - \alpha x}, \qquad \mathcal{D}_3(t) = \varpi e^{-(\mathbf{\Gamma} - \alpha x)}.$$

The essential part of the integral (20) is the Dirac delta function $\delta(\omega - \beta_j)$ caused by the presence of the background $\psi_0^{(j)}$. We will omit it in further calculations. The nontrivial part of the integral (20) is

$$\mathcal{I} = \frac{1}{2\pi} \int_{-\infty}^{\infty} \psi_a(x, t) e^{-i\omega x} dx. \qquad (23)$$

The integral in (23) can be calculated analytically using a residue theorem, namely, $\mathcal{I} = 2\pi i \mathcal{R}$, where $\mathcal{R}$ is the residue of the corresponding singularity of ψ_a in x. The function ψ_a has two singularities at the points x_1 and x_2 which are given by

$$x_1 = \frac{1}{\alpha} \ln \left[\frac{1}{2\mathcal{D}_2} \left(-\mathcal{D}_1 - \sqrt{\mathcal{D}_1^2 - 4\mathcal{D}_2\mathcal{D}_3} \right) \right], \qquad (24)$$

$$x_2 = \frac{1}{\alpha} \ln \left[\frac{1}{2\mathcal{D}_2} \left(-\mathcal{D}_1 + \sqrt{\mathcal{D}_1^2 - 4\mathcal{D}_2\mathcal{D}_3} \right) \right]. \qquad (25)$$

The explicit expressions for the corresponding residues $\mathcal{R}_{x_1}$ and $\mathcal{R}_{x_2}$ at $x = x_1$ and $x = x_2$ are given by

$$\mathcal{R}_{x_1} = \frac{1}{2\pi\alpha\mathcal{D}_2\mathcal{X}} \left(\frac{\mathcal{H} + \mathcal{P}}{\mathcal{D}_1 + \mathcal{X}} \right) e^{-i\omega x_1}, \qquad (26)$$

$$\mathcal{R}_{x_2} = \frac{1}{2\pi\alpha\mathcal{D}_2\mathcal{X}} \left(\frac{\mathcal{H} - \mathcal{P}}{\mathcal{D}_1 - \mathcal{X}} \right) e^{-i\omega x_2}, \qquad (27)$$

where

$$\mathcal{X} = \sqrt{\mathcal{D}_1^2 - 4\mathcal{D}_2\mathcal{D}_3},$$

$$\mathcal{H} = (\mathcal{D}_1\mathcal{B}_2 - \mathcal{D}_2\mathcal{B}_1)\mathcal{X},$$

$$\mathcal{P} = \mathcal{D}_1(\mathcal{D}_1\mathcal{B}_2 - \mathcal{D}_2\mathcal{B}_1) + 2\mathcal{D}_2(\mathcal{D}_2\mathcal{B}_3 - \mathcal{D}_3\mathcal{B}_2).$$

The point x_1 is located on the lower complex plane, while the point x_2 is on the upper complex plane. This means that $\mathcal{I} = 2\pi i \mathcal{R}_{x_1}$ when $\omega > 0$, while $\mathcal{I} = 2\pi i \mathcal{R}_{x_2}$ when $\omega < 0$. Thus, the exact analytic expressions of the KMS spectra can be written as

$$A_\omega^{(j)}(\omega, t) = i \frac{\mathcal{H} + \mathcal{P}}{\alpha\mathcal{D}_2\mathcal{X}(\mathcal{D}_1 + \mathcal{X}^2)} e^{-i\omega x_1}, \quad \omega > 0,$$

$$A_\omega^{(j)}(\omega, t) = i \frac{\mathcal{H} - \mathcal{P}}{\alpha\mathcal{D}_2\mathcal{X}(\mathcal{D}_1 - \mathcal{X}^2)} e^{-i\omega x_2}, \quad \omega < 0. \qquad (28)$$

Figure 2(a) shows the spectral evolution of the vector bright-dark KMS given by Eqs. (28) with $\omega' = \omega - \beta_j$. The spectra correspond to the amplitude profiles shown in Fig. 1(c). In each component, the spectrum is periodic along the t axis just like the KMS itself. The spectra are widest at the points of the maximal self-compression of the soliton. We have compared the exact spectra with the numerical results obtained by the numerical integration for the wave fields factored by a super-Gaussian function. As shown in Fig. 2(b), the spectral profiles are very close to each other.

IV. EIGENVALUE ANALYSIS, KMS EXISTENCE DIAGRAMS, AND CRITICAL RELATIVE WAVE NUMBER

All examples shown in Fig. 1 correspond to the solution (2) with a single eigenvalue (i.e., χ_1). However, Eq. (9) admits multiple roots. The presence of several eigenvalues adds different physics to the KMS in a Manakov system. For
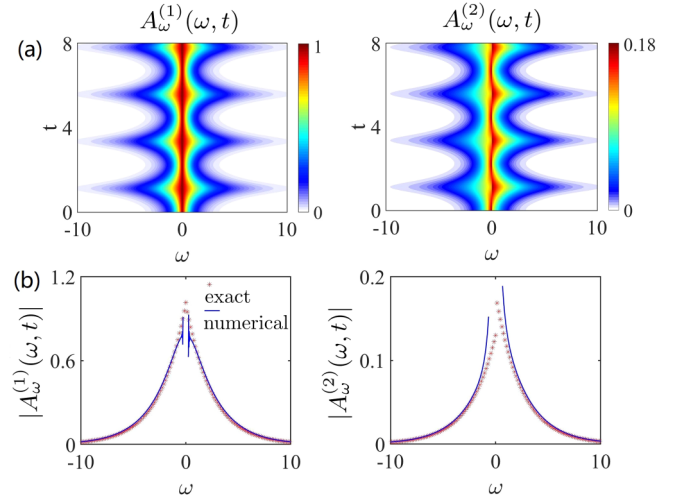

FIG. 2. (a) Evolution of the two spectral components $|A_\omega^{(j)}(\omega, t)|$ of vector KMSs given by Eqs. (28) when $\omega' = \omega - \beta_j$. These spectra correspond to the KMS solution shown in Fig. 1(c). (b) Comparison of numerical (solid curves) and exact (dotted curves) data at the point of the widest spectra ($t \approx 1$).

simplicity, we consider only the case of equal background amplitudes $a_1 = a_2 = a$. Then there are four eigenvalues

$$\chi_1 = -\frac{i}{2}\alpha - \sqrt{\kappa - \sqrt{\eta}}, \quad \chi_2 = -\frac{i}{2}\alpha + \sqrt{\kappa - \sqrt{\eta}},$$

$$\chi_3 = -\frac{i}{2}\alpha - \sqrt{\kappa + \sqrt{\eta}}, \quad \chi_4 = -\frac{i}{2}\alpha + \sqrt{\kappa + \sqrt{\eta}}, \qquad (29)$$

where

$$\kappa = \beta^2 - a^2 - \frac{\alpha^2}{4},$$

$$\eta = a^4 - 4a^2\beta^2 - \alpha^2\beta^2.$$

Naturally, the solution (2) with either of the eigenvalues (29) satisfies the Manakov system (1). However, not all four solutions are realistic. Figure 3 shows the regions of existence of four-vector KMSs with different eigenvalues on the (α, β) plane. The pink, yellow, and cyan areas on these plots correspond to dark, four-petal, and bright KMSs, respectively. These are defined by Eq. (19) as described above. The dashed and solid curves separate the regions of different types of solitons. The solid curves are found analytically, while the dashed curves are calculated numerically.

The analytic expressions for the solid curves can be obtained directly from Eq. (29) using the condition $\eta = 0$. These are given by

$$\beta^2 = \beta_c^2 = \frac{a^4}{4a^2 + \alpha^2}. \qquad (30)$$

This equation defines the critical relative wave number that plays a key role in the properties of the vector KMS. It is represented by two solid lines in Fig. 3. Namely, the KMSs are different in the regions $\beta^2 \leqslant \beta_c^2$ and $\beta^2 > \beta_c^2$.
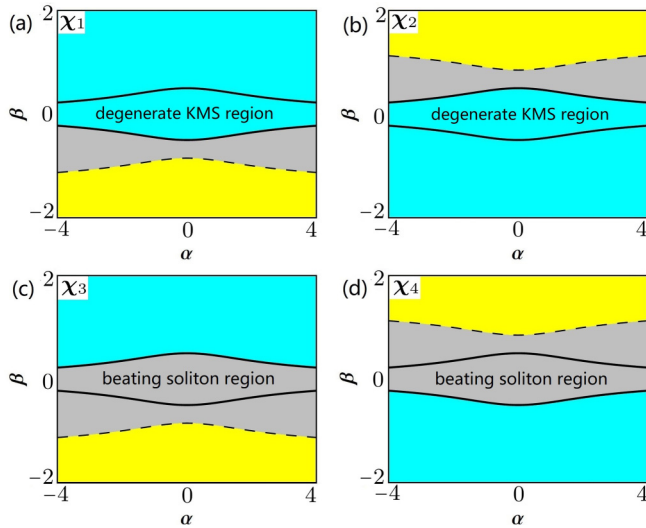
FIG. 3. Existence diagrams of vector KMSs with four eigenvalues (29) in the (α, β) plane. In all panels, cyan, yellow, and gray areas denote the bright, dark, and four-petal KMSs, respectively. The two solid lines in each panel represent the critical condition (30). For (a) χ_1 and (b) χ_2, KMSs are degenerate in the regions within these two lines ($\beta^2 \leqslant \beta_c^2$). The KMSs outside these areas $\beta^2 > \beta_c^2$ are nondegenerate. For (c) χ_3 and (d) χ_4, beating solitons are obtained in the regions $\beta^2 \leqslant \beta_c^2$. Outside these areas, KMSs are the same as those in the cases for χ_1 and χ_2.

A. The KMS in the case $\beta^2 \leqslant \beta_c^2$

When $\beta^2 \leqslant \beta_c^2$, the eigenvalues (29) and the corresponding Lax spectral parameters are purely imaginary. This means that the wave propagates along t with the vanishing group velocity $V_g = 0$. Moreover, we have

$$\chi_{1i} + \chi_{2i} = -\alpha, \qquad (31)$$

$$\chi_{3i} + \chi_{4i} = -\alpha. \qquad (32)$$

These relations satisfy the symmetry (15):

$$\left| \psi_1^{(j)}[(x,t); \chi_1] \right| = \left| \psi_1^{(j)}[(x',t'); \chi_2] \right|, \qquad (33)$$

$$\left| \psi_1^{(j)}[(x,t); \chi_3] \right| = \left| \psi_1^{(j)}[(x',t'); \chi_4] \right|. \qquad (34)$$

This indicates that $\{\psi_1^{(j)}(\chi_1), \psi_1^{(j)}(\chi_2)\}$ or $\{\psi_1^{(j)}(\chi_3), \psi_1^{(j)}(\chi_4)\}$ have the same amplitude profiles. The only difference between them is the trivial shifts in x and t equal to Δx and Δt. Figures 4(a) and 4(b) confirm this. These figures also show that the two upper profiles $|\psi_1^{(j)}(\chi_1)|$ and $|\psi_1^{(j)}(\chi_2)|$ are the conventional bright KMS structures, while the profiles $|\psi_1^{(j)}(\chi_3)|$ and $|\psi_1^{(j)}(\chi_4)|$ are the four-petal ones.

Importantly, when $\beta^2 \leqslant \beta_c^2$, the solutions $\psi_1^{(j)}(\chi_3)$ and $\psi_1^{(j)}(\chi_4)$ are not KMSs which are formed by the interaction between solitons and plane waves. In order to elucidate this point, let us consider the limit $\beta \to 0$. When the Manakov system (1) decouples at $\beta \to 0$, only solutions $\psi_1^{(j)}(\chi_1)$ and $\psi_1^{(j)}(\chi_2)$ become scalar (bright) KMSs [see Fig. 4(a)]. In the

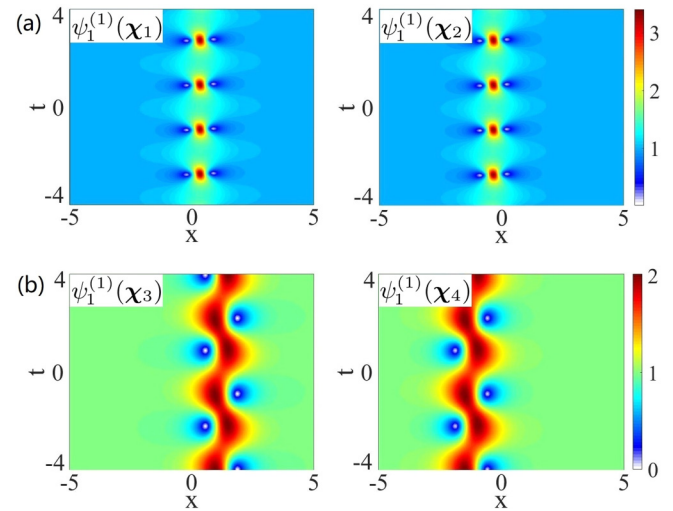limit $\beta = 0$ we have

$$\psi_1^{(1)} = \psi_1^{(2)} \quad \text{for } \chi_1, \chi_2. \qquad (35)$$

The relation (35) is the reduction of the vector solution to the scalar KMS. Figure 5(a) shows the amplitude profiles of the decoupled KMSs when the eigenvalue χ_1 is chosen. We can see that this solution is a scalar KMS.

FIG. 4. Amplitude profiles of $|\psi_1^{(1)}|$ in the region $\beta^2 \leqslant \beta_c^2$ with different eigenvalues (29). The parameters are $a = 1, \alpha = 2$, and $\beta = 0.1$.
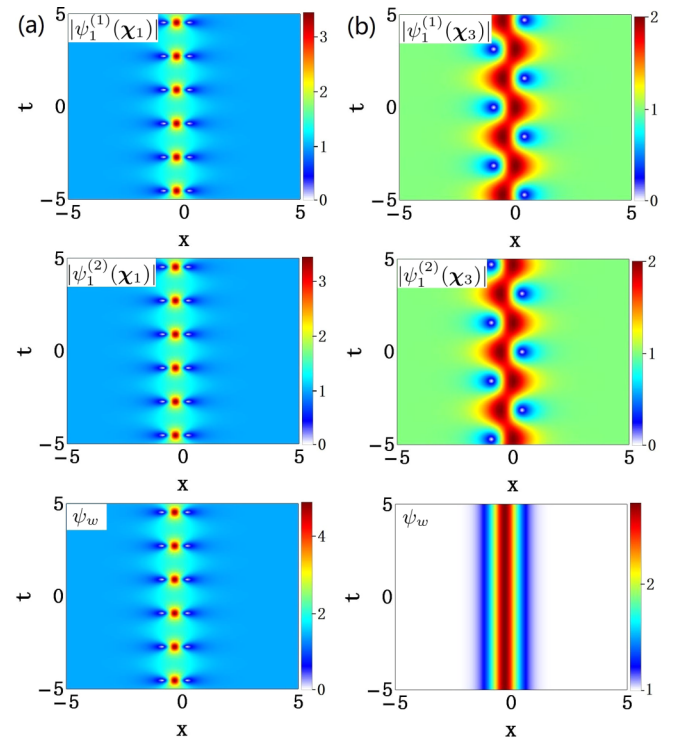

FIG. 5. Amplitude profiles $|\psi_1^{(j)}|$ and the total intensity distributions $\psi_w = \sqrt{|\psi_1^{(1)}|^2 + |\psi_1^{(2)}|^2}$ when $\beta = 0$ with the eigenvalues (a) χ_1 and (b) χ_3. The other parameters are the same as in Fig. 4.

On the other hand, the solutions $\psi_1^{(j)}(\chi_3)$ and $\psi_1^{(j)}(\chi_4)$ have the four-petal amplitude patterns when $\beta^2 \leqslant \beta_c^2$. Such solutions cannot be reduced to the scalar ones in the limit $\beta = 0$:

$$\psi_1^{(1)} \neq \psi_1^{(2)} \quad \text{for } \chi_3, \chi_4. \tag{36}$$

In this limit, the solutions $\psi_1^{(j)}(\chi_3)$ and $\psi_1^{(j)}(\chi_4)$ have the form

$$\psi_1^{(j)}(\chi_3) = \psi_0^{(j)}(\psi_{DS} \mp \psi_{BS}), \tag{37}$$

$$\psi_1^{(j)}(\chi_4) = \psi_0^{(j)}(\tilde\psi_{DS} \mp \tilde\psi_{BS}), \tag{38}$$

where

$$\tilde\psi_{DS} = \psi_{DS}(-x), \quad \tilde\psi_{BS} = -\psi_{BS}(-x) \tag{39}$$

and

$$\psi_{DS} = -\frac{(4a^2 + \alpha^2)\sinh(\alpha x) + \alpha^2 \cosh(\alpha x)}{(4a^2 + \alpha^2)\cosh(\alpha x) + \alpha^2 \sinh(\alpha x)}, \tag{40}$$

$$\psi_{BS} = \frac{2(2a^2 + \alpha^2)\exp\left(\frac{1}{2}i\alpha^2 t\right)}{(4a^2 + \alpha^2)\cosh(\alpha x) + \alpha^2 \sinh(\alpha x)}. \tag{41}$$

These solutions can be considered as linear superpositions of the dark and bright solitons (ψ_{DS}, ψ_{BS}, $\tilde\psi_{DS}$, and $\tilde\psi_{BS}$). These are different from the multisoliton complexes, which are the nonlinear superpositions of several fundamental solitons [57,58]. Figure 5(b) gives an example showing that such a solution is the result of the beating effect of vector solitons with the oscillation frequency $\alpha^2/2$ along the t axis. The total intensity $\psi_w = \sqrt{|\psi_1^{(1)}|^2 + |\psi_1^{(2)}|^2}$ shows an antidark soliton profile. Similar solutions can be obtained by SU(2) rotations of vector dark-bright solitons [59–61].

Thus, the solutions $\psi_1^{(j)}(\chi_3)$ and $\psi_1^{(j)}(\chi_4)$ are vector solitons in the region $\beta^2 \leqslant \beta_c^2$ which can be interpreted as the result of linear interference between the dark and bright solitons. Only the solutions $\psi_1^{(j)}(\chi_1)$ and $\psi_1^{(j)}(\chi_2)$ are KMSs which are formed by the interaction between solitons and plane waves when $\beta^2 \leqslant \beta_c^2$. Moreover, for any fixed set of parameters (a, β, and α), the solutions $\psi_1^{(j)}(\chi_1)$ and $\psi_1^{(j)}(\chi_2)$ are degenerate KMBs.

B. Nondegenerate KMSs in the case $\beta^2 > \beta_c^2$

In the case $\beta^2 > \beta_c^2$, all four eigenvalues are valid and satisfy the relations

$$\chi_{1i} + \chi_{3i} = -\alpha, \quad \chi_{2i} + \chi_{4i} = -\alpha, \tag{42}$$

$$\chi_{1r} = \chi_{3r} = -\chi_{2r} = -\chi_{4r}. \tag{43}$$

The symmetry (15) leads to

$$\left|\psi_1^{(j)}[(x,t);\chi_1]\right| = \left|\psi_1^{(j)}[(x',t');\chi_3]\right|, \tag{44}$$

$$\left|\psi_1^{(j)}[(x,t);\chi_2]\right| = \left|\psi_1^{(j)}[(x',t');\chi_4]\right|, \tag{45}$$

but

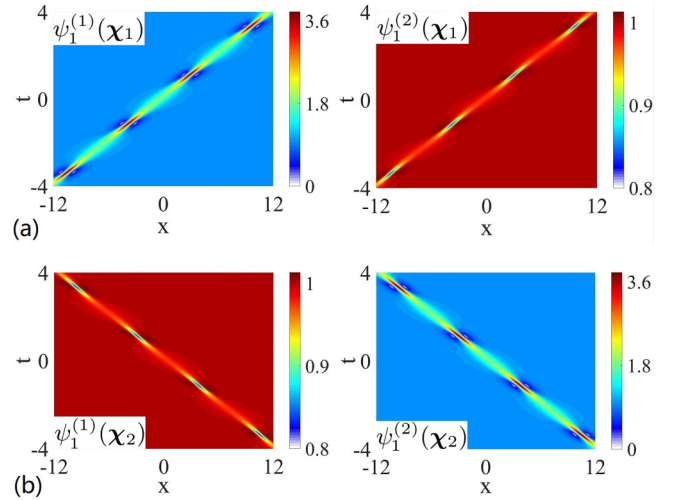$$\left|\psi_1^{(j)}[(x,t);\chi_1]\right| \neq \left|\psi_1^{(j)}[(x,t);\chi_2]\right|. \tag{46}$$

FIG. 6. Amplitude profiles of the vector KMSs $|\psi_1^{(j)}|$ with the eigenvalues (a) χ_1 and (b) χ_2, in the region $\beta^2 > \beta_c^2$. The parameters are the same as in Fig. 4, except for $\beta = 3$.

It follows, from Eqs. (44)–(46), that for any fixed set of parameters (a, β, and α) there are only two different types of vector KMSs in the region $\beta^2 > \beta_c^2$. Such complexity of KMSs is absent in the scalar case.

Figure 6 shows the wave profiles of KMSs $\psi^{(j)}(\chi_1)$ and $\psi^{(j)}(\chi_2)$ in the region $\beta^2 > \beta_c^2$. The first solution is a bright-dark soliton pair shown in Fig. 6(a). It is propagating to the right with the group velocity $V_g = -\chi_r$ according to Eq. (43). The second solution is dark-bright soliton pair shown in Fig. 6(b). It is propagating to the left with the same group velocity $V_g = -\chi_r$. They have the same period $\Omega/2\pi$ along t and the same width ($\sim 1/\alpha$) along x.

V. MULTIPLE KMSS IN THE REGION $\beta^2 > \beta_c^2$

Each of the vector KMSs can be part of the nonlinear superposition of more complex solutions. The superposition of several KMSs can be constructed via the Darboux transformation as shown in the Appendices. In the NLSE case, such superpositions have been constructed in [62]. Here we concentrate on the solutions which do not have analogs in the scalar NLSE case. Namely, we consider the multiple KMSs in the region $\beta^2 > \beta_c^2$ corresponding to the eigenvalues χ_1 and χ_2 given by Eq. (29).

Figure 7 shows the interaction of the two KMSs shown in Fig. 6 positioned on the same plane-wave background. The two KMSs propagate with opposite group velocities interacting at the time $t = 0$. An interesting finding is that such interaction do not induce any amplitude enhancement at the point of the intersection. The two solitons pass through each other without visible mutual influence when crossing each other. This is in sharp contrast to the interaction between the scalar KMSs [62].

The comparison of the amplitude profiles of a single soliton and the two-soliton solution at $t = 0$ in Fig. 7(b) shows their complete overlapping. On the other hand, the phase jump of the two-soliton interaction at $t = 0$ shown in the lower part of Fig. 7(b) is a simple sum of the phase
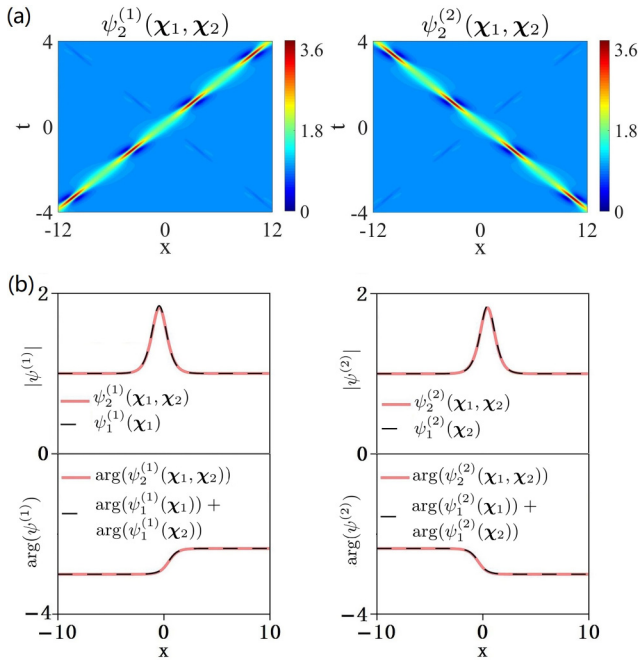
FIG. 7. (a) Amplitude profiles of the second-order KMSs $|\psi_2^{(j)}|$. The plot shows the interaction of the two fundamental solitons in Fig. 6 placed on the same background. (b) Comparison of the amplitude (upper plots) and phase (lower plots) profiles of the second-order and the first-order solutions at $t = 0$. The parameters are the same as in Fig. 6.

of each KMS shown in Fig. 6. The amplitude and phase profiles shown in Fig. 7(b) may serve as the initial conditions for the excitation of such a solution in numerical simulations.

More possibilities can be realized when we consider the second-order KMS solution corresponding to the eigenvalues χ_1 and χ_2 with different α in the region $\beta^2 > \beta_c^2$. Figure 8 shows the fourth-order KMS formed by two pairs of vector fundamental solitons corresponding to the eigenvalues χ_1 and χ_2 with $\alpha = 2$ and 2.1. The plot shows two pairs of bright-dark KMSs in each of the $\psi^{(1)}$ and $\psi^{(2)}$ wave components. The group velocities of each pair of KMSs are opposite, leading to the collision of the group of the KMSs at $t = 0$.
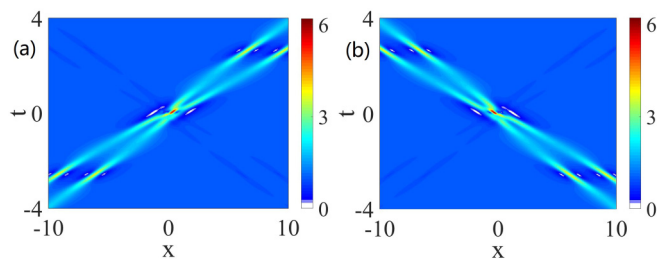

FIG. 8. Amplitude profiles (a) $|\psi_4^{(1)}|$ and (b) $|\psi_4^{(2)}|$ of the fourth-order solution that involves four intersecting KMSs with the eigenvalues χ_1 and χ_2 given by Eq. (29) and $\alpha = 2$ and 2.1, respectively. The other parameters are the same as in Fig. 7.
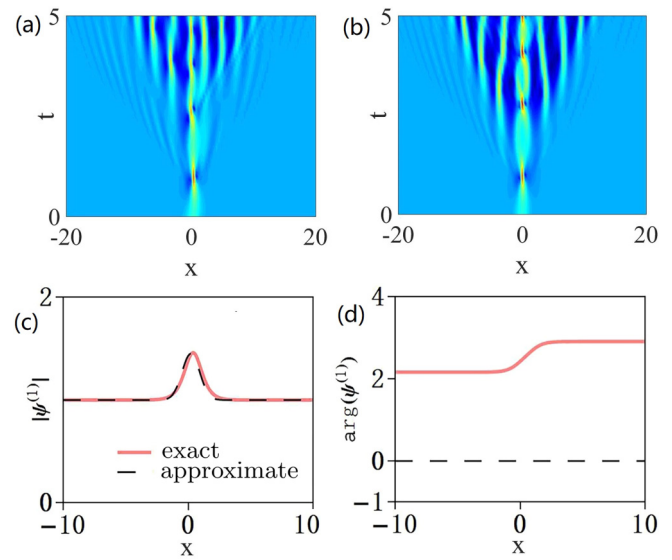

FIG. 9. Numerical simulations starting from (a) the exact initial condition (2) at $t = 0$ and (b) an approximation (47). The parameter β is chosen in the region $\beta^2 \leqslant \beta_c^2$. (c) Amplitude profiles of the exact (red solid curve) and approximate (black dashed curve) initial conditions. (d) Phase profiles of the same initial conditions.

VI. NUMERICAL SIMULATIONS

From an experimental point of view, an important question is what type of initial conditions can create the vector KMS that we have derived above. Clearly, our exact solution (2) provides an ideal initial condition at any given t. A convenient choice is $t = 0$. Then, if we use $\psi^{(j)}(x, t = 0)$ as the initial condition, both degenerate or nondegenerate KMSs can be excited. Another possibility is to use approximations that are relatively close to the exact solution. Below we used the expression

$$\psi^{(j)} = \psi_0^{(j)}[1 + \mathcal{L}^{(j)}(x/w)], \qquad (47)$$

where the localized perturbation $\mathcal{L}^{(j)}(x/w)$ is either the sech or Gaussian function with w its width. Without loss of generality, we use a Gaussian function

$$\mathcal{L}^{(j)} = s^{(j)} \exp(-x^2/w^2) \exp(i\theta), \qquad (48)$$

where $s^{(j)}$ and θ are the amplitudes and the phase, respectively. We choose the width of the localized perturbation w close to that of our exact solutions, $w \sim 1/\alpha$.

Figure 9 depicts numerical simulations of the KMS in the first component $\psi^{(1)}$ that started with the exact initial conditions given by the solution (2) [Fig. 9(a)] and the approximate initial condition (47) [Fig. 9(b)]. Simulations are done for the region $\beta^2 \leqslant \beta_c^2$. The amplitude profiles shown in Fig. 9(c) are similar in each case. However, the phase profiles shown in Fig. 9(d) are different.

The fundamental KMS in each case is excited initially. However, the background is unstable and modulations around the KMS appear soon after the propagation starts. The latter is known as the automodulation that appears spontaneously from a localized initial modulation [63–65]. Such additional modulation has been observed also in the case of the scalar NLSE [66]. This means that the clean observation of the KMS
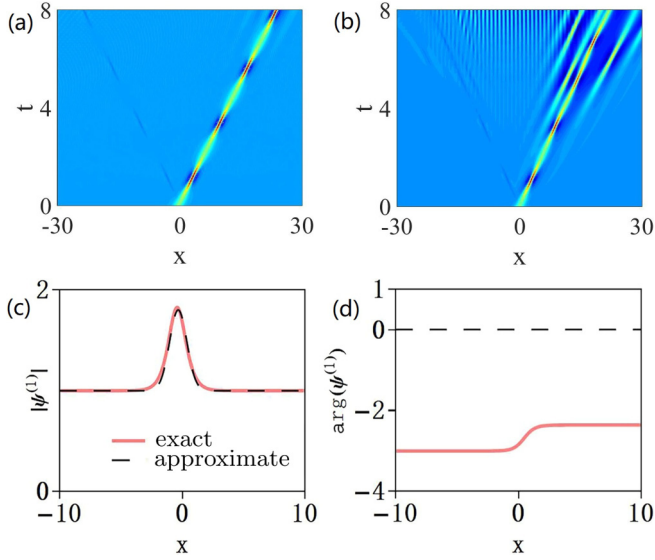
FIG. 10. Numerical simulations starting from (a) the exact initial condition (2) at $t = 0$ and (b) an approximation (47). The parameter β is chosen in the region $\beta^2 > \beta_c^2$. (c) Amplitude profiles of the exact (red solid curve) and approximate (black dashed curve) initial conditions. (d) Phase profiles of the same initial conditions.

in experiments would be difficult. The experimental observations of the scalar KMS in an optical fiber are based on purely periodic modulation [26]. Such a technique may prevent the appearance of the automodulation patterns.

Next we consider numerical simulations of the KMS in the region $\beta^2 > \beta_c^2$. The exact and approximate initial conditions that we use here are the same as in Fig. 9. The results of numerical simulations of the KMS in this case are shown in Figs. 10(a) and 10(b). In each case, instead of one KMS, two KMSs propagating with opposite group velocities are excited. Numerical simulations in Fig. 10(a) started with the exact initial condition show very good agreement with the exact results presented in Fig. 7(a). Remarkably, the automodulation in this case is very weak and can be seen only after four KMS periods of propagation. Approximate initial conditions, on the contrary, lead to the quick appearance of the modulation pattern, as can be seen in Fig. 10(b). This means that accurate initial conditions provide a better way of excitation of nondegenerate KMSs in experiments.

VII. TRANSFORMATION OF THE VECTOR KMS TO AN ORDINARY SOLITON

In the NLSE case, the KMS becomes a standard bright soliton at the zero amplitude of the background wave [24]. A similar transformation occurs in the case of the vector KMS. This can be demonstrated directly using the exact solution (2) by adjusting the corresponding parameters. Below we establish the link between the vector KMS and an ordinary soliton by considering the condition of degeneracy of the eigenvalues. Indeed, the ordinary soliton formation can be extracted from the analysis of the eigenvalues (9). Alternatively, the plain soliton solutions can be independently derived using the Darboux transformation. The details are given in Appendix B.

For solitons of the Manakov system (1), there are two backgrounds. Therefore, the two cases can be considered separately. These are (i) $a_1 = a_2 = 0$ and (ii) $a_1 \neq 0$ and $a_2 = 0$. We will show that in case (i), the vector KMS is reduced to a nondegenerate bright soliton with opposite velocities of the two components. However, case (ii) reveals a qualitatively different type of nondegenerate localized waves. Let us consider these two cases in detail.

A. Nondegenerate bright solitons with $a_1 = a_2 = 0$

From Eq. (10) we can see that the spectral parameter is

$$\lambda = \chi. \tag{49}$$

The resulting eigenvalues (29) are

$$\chi_1 = -\beta, \quad \chi_2 = -i\alpha + \beta,$$
$$\chi_4 = +\beta, \quad \chi_3 = -i\alpha - \beta. \tag{50}$$

Among them, only the complex eigenvalues χ_2 and χ_3 are valid. Each of these two eigenvalues leads to the fundamental vector bright soliton.

However, a nontrivial finding is that the second-order solution with the same eigenvalues χ_2 and χ_3 is a different family of nondegenerate bright solitons. The derivation of these solutions is presented in Appendix B 1. The final result is

$$\psi_2^{(j)} = \frac{\mathcal{T}[(\alpha + 2i\beta)\cosh(\kappa_j) - \alpha \sinh(\kappa_j)]e^{i\phi_j}}{\mathcal{G}\cosh(2\alpha\beta t) + \mathcal{N}\cosh(2\alpha x) - \alpha^2 \sinh(2\alpha x)}, \tag{51}$$

where the values κ_j and ϕ_j are given by

$$\kappa_j = \alpha(x \pm \beta t), \quad \phi_j = \tfrac{1}{2}(\beta^2 - \alpha^2)t \pm \beta x$$

and the coefficients $\mathcal{T}$, $\mathcal{G}$, and $\mathcal{N}$ are

$$\mathcal{T} = 2\alpha(i\alpha + \beta), \quad \mathcal{G} = 2(\alpha^2 + \beta^2), \quad \mathcal{N} = \alpha^2 + 2\beta^2.$$

Figure 11(a) shows the amplitude profiles of the nondegenerate vector solitons given by Eq. (51). The distinctive feature of this solution is that there is only one soliton in each wave component. However, solitons in different wave components have opposite group velocities. This can also be seen from the expression for κ_j in (51).

A more detailed comparison of the second-order soliton solution with a limiting case of the second-order KMS is provided in Fig. 11. Figure 11(a) shows the nondegenerate second-order soliton solution, while Fig. 11(b) shows the second-order KMS solution in the limiting case of $a_1 \to 0$ and $a_2 \to 0$. This is the same solution as in Fig. 7 but in the limit of zero background. As expected, the plots in Figs. 11(a) and 11(b) are identical. A comparison of the soliton profiles at the point $t = 0$ confirms additionally that the two second-order solutions have the same profiles. Interestingly, there is no visible interaction between the two solitons.

More complex patterns can be revealed from the fourth-order solutions derived in Appendix B 1. Figure 12(a) displays the two wave components of the fourth-order soliton solution with the eigenvalues χ_2 and χ_3 where $\alpha = 2$ and 2.1, respectively. These patterns show the interaction between the nondegenerate solitons. However, only two solitons interact
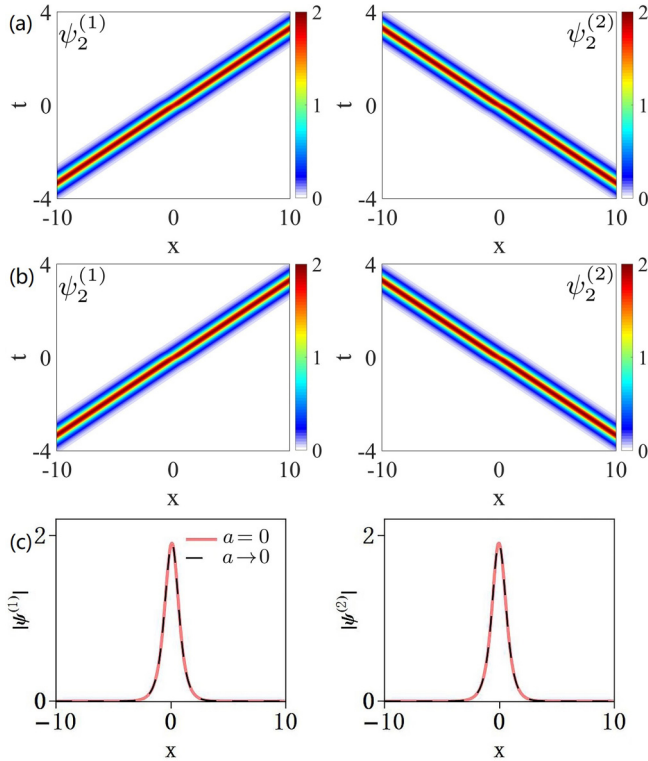
FIG. 11. (a) Amplitude profiles of nondegenerate solitons given by Eq. (51), with $\beta = 3$ and $\alpha = 2$. (b) Amplitude profiles of nondegenerate KMSs in the limiting case $a_1 = a_2 = a \to 0$. We use $a = 10^{-4}$ in the solutions shown in Fig. 7. (c) Comparison of the soliton profiles shown in (a) and (b) at $t = 0$.

with each other in each wave component. Again, there is no interaction between different wave components, although the two pairs of solitons have opposite velocities and collide at the point $t = 0$.

The same fourth-order soliton solution can be obtained as the limiting case of the fourth-order KMS solution shown in Fig. 8 but when $a_1 \to 0$ and $a_2 \to 0$. This solution is shown in Fig. 12(b). The two fourth-order solutions shown in Figs. 12(a) and 12(b) are identical. This can also be seen from the comparison of the soliton profiles at $t = 0$ shown in Fig. 12(c).

B. Nondegenerate localized waves with $a_1 \neq 0$ and $a_2 = 0$

When $a_1 \neq 0$ and $a_2 = 0$, the spectral parameter defined by Eq. (10) is

$$\lambda = \chi - \frac{a_1^2}{\chi + \beta_1}. \tag{52}$$

The corresponding eigenvalues χ are obtained explicitly from Eq. (9):

$$\chi_1 = -\beta_1 - \frac{i}{2}\alpha + \frac{i}{2}\sqrt{4a_1^2 + \alpha^2}, \quad \chi_2 = -\beta_2 - i\alpha,$$

$$\chi_3 = -\beta_1 - \frac{i}{2}\alpha - \frac{i}{2}\sqrt{4a_1^2 + \alpha^2}, \quad \chi_4 = -\beta_2. \tag{53}$$

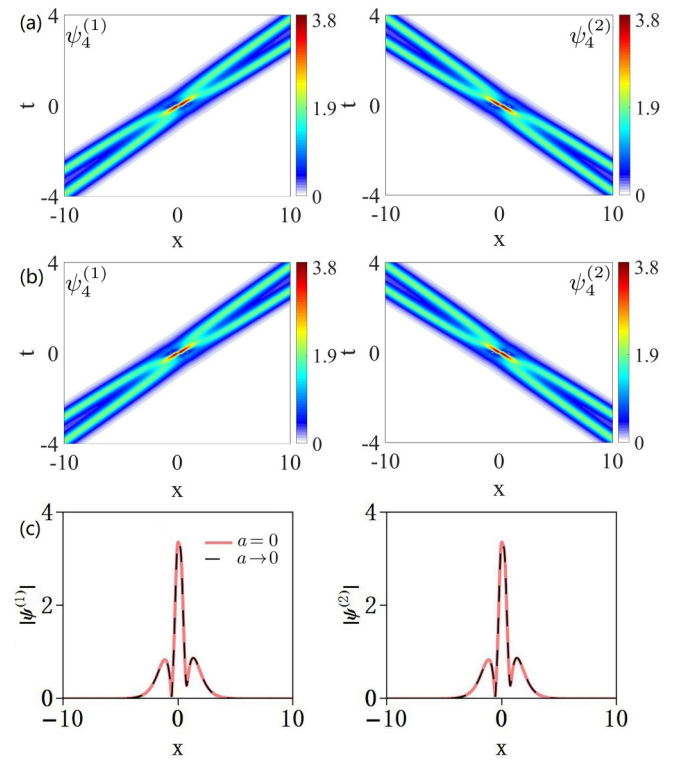Here the three complex eigenvalues χ_1, χ_2, and χ_3 are valid.

FIG. 12. (a) Amplitude profiles of nondegenerate fourth-order solutions given by Eqs. (B3) and (B4), with $\beta = 3$, $\alpha = 2$, and $\alpha = 2.1$. (b) Amplitude profiles of the two second-order nondegenerate KMSs. These are limiting cases of the solutions shown in Fig. 8 when $a_1 = a_2 = a \to 0$. In order to avoid numerical artifacts, we use $a_1 = a_2 = 10^{-4}$. (c) Comparison of the wave profiles shown in (a) and (b) at the point $t = 0$.

The use of only χ_1 or χ_3 as the eigenvalue in the first step of Darboux transformation leads to a bright KMS in the $\psi^{(1)}$ wave component and a zero solution in $\psi^{(2)}$. This solution is given by Eq. (B15). It is the KMS solution of the nonlinear Schrödinger equation. As

$$\chi_{1i} + \chi_{3i} = -\alpha, \quad \chi_{1r} = \chi_{3r}. \tag{54}$$

the use of either of χ_1 or χ_3 leads to the same result. On the other hand, the use of χ_2 as the eigenvalue in the first step of Darboux transformation results in the exact solution in the form of the vector dark-bright soliton.

The second step of the Darboux transformation with the use of the eigenvalues χ_1 (or χ_3) and χ_2 results in more complex vector localized waves. The corresponding exact solutions are presented in Appendix B 2. Figure 13 shows examples of amplitude profiles of these solutions for particular values of β and α. Figure 13(a) corresponds to the KMS in the first wave component and a bright soliton in the second component moving with the opposite group velocity. The same solution can be obtained from the one shown in Fig. 7 in the limit $a_2 \to 0$. The corresponding amplitude profile is shown in Fig. 13(b). Naturally, the profiles shown in Figs. 13(a) and 13(b) are identical. More evidence comes from the comparison of the wave profiles of the solutions shown in Figs. 13(a) and 13(b) at $t = 0$. This is shown in Fig. 13(c). The two profiles completely overlap.
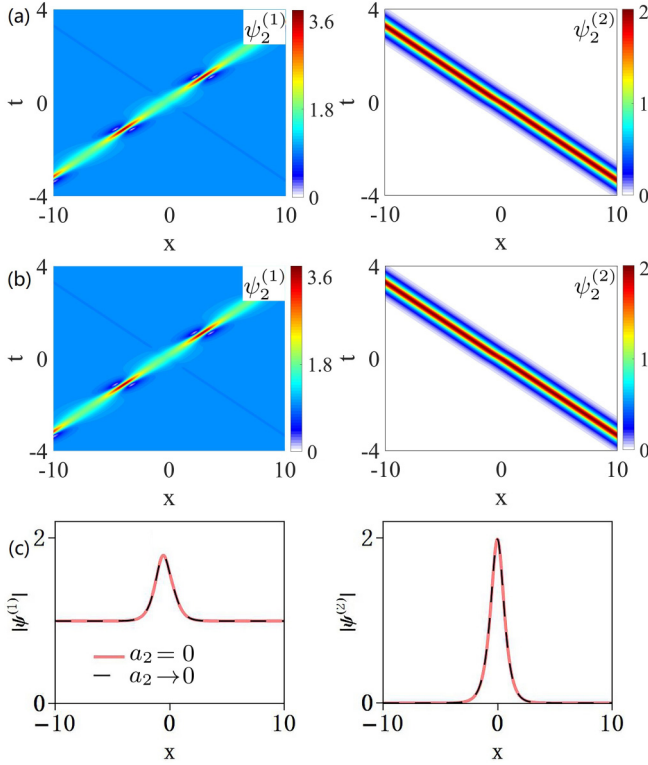
FIG. 13. (a) Amplitude profiles of nondegenerate solitons given by Eq. (51), with $\beta = 3$ and $\alpha = 2$. (b) Amplitude profiles of nondegenerate KMSs in the limiting case of $a_1 = 1$ and $a_2 \to 0$ (we use here $a_2 = 10^{-4}$). This is a limiting case of the KMS shown in Fig. 7. (c) Comparison of the profiles shown in (a) and (b) at $t = 0$.

The wave profile shown in Fig. 13(c) can be used as the initial condition for the excitation of nondegenerate waves. Such simulations will provide an independent way of proving the validity of solutions. Figure 14 shows the results of the simulations. As we can see from this figure, the nondegenerate waves are well reproduced. Namely, the results are basically the same as shown in Figs. 13(a) and 13(b). The KMS is excited in the first component, while the bright soliton with the opposite group velocity is excited in the second component.

VIII. CONCLUSION

We have presented theoretical and numerical studies of vector KMSs for the Manakov equations. We derived a gen-
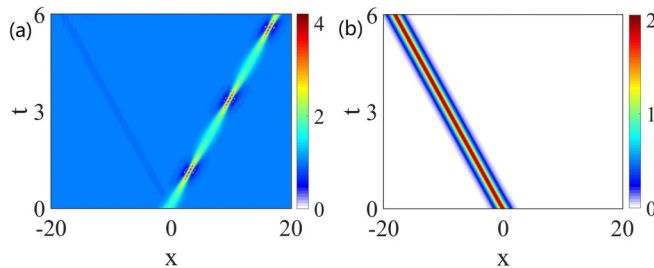

FIG. 14. Numerical simulations of nondegenerate waves starting with the initial condition shown in Fig. 13(c) with $a_2 = 0$. (a) and (b) are the two components of the field.

eral family of exact vector KMS solutions of the first and higher (up to the fourth) orders that cannot be reduced to the solutions of the scalar NLSE. Solutions that we derived can be useful for experimental works in optics, hydrodynamics, and cold-atom physics. One of our nontrivial findings is the prediction of a different class of nondegenerate KMSs. They appear as higher-order solutions of the Manakov equations that form a nonlinear superposition of fundamental KMSs. We provided the amplitude profiles for such solutions and their physical spectra and confirmed our exact solutions by numerical simulations. We also considered the limiting case of zero background when the KMS is reduced to ordinary soliton solutions. This way, we found two different families of nondegenerate solitons.

APPENDIX A: VECTOR KMS SOLUTIONS

We represent Eqs. (1) as the condition of compatibility of two linear equations with 3×3 matrix operators

$$\mathbf{\Psi}_x = \mathbf{U}\Psi, \quad \mathbf{\Psi}_t = \mathbf{V}\Psi, \tag{A1}$$

where $\mathbf{\Psi} = (R, S, W)^{\mathsf{T}}$ (T means a matrix transpose) and

$$\mathbf{U} = i \begin{pmatrix} \lambda & \psi^{(1)*} & \psi^{(2)*} \\ \psi^{(1)} & 0 & 0 \\ \psi^{(2)} & 0 & 0 \end{pmatrix}, \tag{A2}$$

$$\mathbf{V} = i\frac{\mathbf{U}^2}{2} + i \begin{pmatrix} \mathbf{a}^2 + \lambda^2 & \psi^{(1)*}\lambda & \psi^{(2)*}\lambda \\ \psi^{(1)}\lambda & \mathbf{a}^2 + |\psi^{(1)}|^2 & \psi^{(1)}\psi^{(2)*} \\ \psi^{(2)}\lambda & \psi^{(1)*}\psi^{(2)} & \mathbf{a}^2 + |\psi^{(2)}|^2 \end{pmatrix}, \tag{A3}$$

where the asterisk denotes the complex conjugate, λ is the spectral parameter, and $\mathbf{a}^2 = a_1^2 + a_2^2$. The Manakov system (1) is equivalent to the compatibility condition

$$\mathbf{U}_t - \mathbf{V}_x + [\mathbf{U}, \mathbf{V}] = 0. \tag{A4}$$

In order to obtain the fundamental (first-order) vector KMS solution, we start with the vector plane wave (3) $\psi_0^{(j)}$ as the seed solution. The corresponding spectral parameter $\lambda_{[1]}$ should satisfy the relation (10). The related eigenfunctions $(R_{[1]}, S_{[1]}, W_{[1]})$ are given by

$$R_{[1]} = \varphi_{[1]} + \tilde{\varphi}_{[1]}, \tag{A5}$$

$$S_{[1]} = \psi_0^{(1)} \left(\frac{\varphi_{[1]}}{\beta_1 + \boldsymbol{\chi}_{[1]}} + \frac{\tilde{\varphi}_{[1]}}{\beta_1 + \tilde{\boldsymbol{\chi}}_{[1]}} \right), \tag{A6}$$

$$W_{[1]} = \psi_0^{(2)} \left(\frac{\varphi_{[1]}}{\beta_2 + \boldsymbol{\chi}_{[1]}} + \frac{\tilde{\varphi}_{[1]}}{\beta_2 + \tilde{\boldsymbol{\chi}}_{[1]}} \right), \tag{A7}$$

where $\tilde{\boldsymbol{\chi}}_{[1]} = \boldsymbol{\chi}_{[1]} + i\alpha$, with $\boldsymbol{\chi}_{[1]}$ one of the complex roots of Eq. (9). As mentioned above, the choice of $\boldsymbol{\chi}_{[1]}$ is not arbitrary.

For the case $\beta^2 \lesssim \beta_c^2$ shown in Sec. IV, we have to use $\boldsymbol{\chi}_{[1]} = \boldsymbol{\chi}_1$ or $\boldsymbol{\chi}_{[1]} = \boldsymbol{\chi}_2$. Moreover,

$$\varphi_{[1]} = \exp\left[i\boldsymbol{\chi}_{[1]}\left(x + \tfrac{1}{2}\boldsymbol{\chi}_{[1]}t\right)\right], \tag{A8}$$

$$\tilde{\varphi}_{[1]} = \exp\left[i\tilde{\boldsymbol{\chi}}_{[1]}\left(x + \tfrac{1}{2}\tilde{\boldsymbol{\chi}}_{[1]}t\right)\right]. \tag{A9}$$

The fundamental KMS solution is then obtained through the first step of the Darboux transformation:

$$\psi_1^{(1)} = \psi_0^{(1)} + \frac{(\lambda_{[1]}^* - \lambda_{[1]})R_{[1]}^* S_{[1]}}{|R_{[1]}|^2 + |S_{[1]}|^2 + |W_{[1]}|^2},$$
$$\psi_1^{(2)} = \psi_0^{(2)} + \frac{(\lambda_{[1]}^* - \lambda_{[1]})R_{[1]}^* W_{[1]}}{|R_{[1]}|^2 + |S_{[1]}|^2 + |W_{[1]}|^2}. \tag{A10}$$

Equations (A10) lead directly to Eq. (2).

Higher-order KMS solutions can be obtained via the iteration of a Darboux transformation from the fundamental KMS solution (A10). An alternative technique is based on a Bäcklund transformation [46]. After performing the transformation, we obtain the general determinant form of the Nth-order KMS solution

$$\psi_N^{(j)} = \psi_0^{(j)} \frac{\det(M_j)}{\det(M)}, \tag{A11}$$

$$M_j = \left(m_{[k1],[k2]}^{(j)}\right)_{1 \leqslant k1, k2 \leqslant N}, \tag{A12}$$

$$M = \left(m_{[k1],[k2]}\right)_{1 \leqslant k1, k2 \leqslant N}, \tag{A13}$$

where

$$m_{[k1],[k2]} = \frac{\varphi_{[k1]} + \varphi_{[k2]}^*}{\boldsymbol{\chi}_{[k2]}^* - \boldsymbol{\chi}_{[k1]}} + \frac{\tilde{\varphi}_{[k1]} + \tilde{\varphi}_{[k2]}^*}{\tilde{\boldsymbol{\chi}}_{[k2]}^* - \tilde{\boldsymbol{\chi}}_{[k1]}} + \frac{\varphi_{[k1]} + \tilde{\varphi}_{[k2]}^*}{\tilde{\boldsymbol{\chi}}_{[k2]}^* - \boldsymbol{\chi}_{[k1]}}$$
$$+ \frac{\tilde{\varphi}_{[k1]} + \varphi_{[k2]}^*}{\boldsymbol{\chi}_{[k2]}^* - \tilde{\boldsymbol{\chi}}_{[k1]}}, \tag{A14}$$

$$m_{[k1],[k2]}^{(j)} = \frac{\boldsymbol{\chi}_{[k2]}^* + \beta_j}{\boldsymbol{\chi}_{[k1]} + \beta_j} \frac{\varphi_{[k1]} + \varphi_{[k2]}^*}{\boldsymbol{\chi}_{[k2]}^* - \boldsymbol{\chi}_{[k1]}} + \frac{\tilde{\boldsymbol{\chi}}_{[k2]}^* + \beta_j}{\tilde{\boldsymbol{\chi}}_{[k1]} + \beta_j} \frac{\tilde{\varphi}_{[k1]} + \tilde{\varphi}_{[k2]}^*}{\tilde{\boldsymbol{\chi}}_{[k2]}^* - \tilde{\boldsymbol{\chi}}_{[k1]}}$$
$$+ \frac{\tilde{\boldsymbol{\chi}}_{[k2]}^* + \beta_j}{\boldsymbol{\chi}_{[k1]} + \beta_j} \frac{\varphi_{[k1]} + \tilde{\varphi}_{[k2]}^*}{\tilde{\boldsymbol{\chi}}_{[k2]}^* - \boldsymbol{\chi}_{[k1]}}$$
$$+ \frac{\boldsymbol{\chi}_{[k2]}^* + \beta_j}{\tilde{\boldsymbol{\chi}}_{[k1]} + \beta_j} \frac{\tilde{\varphi}_{[k1]} + \varphi_{[k2]}^*}{\boldsymbol{\chi}_{[k2]}^* - \tilde{\boldsymbol{\chi}}_{[k1]}}. \tag{A15}$$

Here $m_{[k1],[k2]}$ and $m_{[k1],[k2]}^{(j)}$ represent the matrix elements of M and M_j in the $(k1)$th row and $(k2)$th column. Moreover, $\tilde{\boldsymbol{\chi}}_{[k1]}(\tilde{\boldsymbol{\chi}}_{[k2]}) = \boldsymbol{\chi}_{[k1]}(\boldsymbol{\chi}_{[k2]}) + i\alpha$ $(k1, k2 = 1, 2, 3, \ldots, N)$, with $\boldsymbol{\chi}_{[k1]}(\boldsymbol{\chi}_{[k2]})$ one of the complex roots of Eq. (9). The function $\varphi_{[k1]}(\varphi_{[k2]})$ is given by

$$\varphi_{[k1]} = \exp\left[i\boldsymbol{\chi}_{[k1]}\left(x + \tfrac{1}{2}\boldsymbol{\chi}_{[k1]}t\right)\right], \tag{A16}$$

$$\tilde{\varphi}_{[k1]} = \exp\left[i\tilde{\boldsymbol{\chi}}_{[k1]}\left(x + \tfrac{1}{2}\tilde{\boldsymbol{\chi}}_{[k1]}t\right)\right], \tag{A17}$$

$$\varphi_{[k2]} = \exp\left[i\boldsymbol{\chi}_{[k2]}\left(x + \tfrac{1}{2}\boldsymbol{\chi}_{[k2]}t\right)\right], \tag{A18}$$

$$\tilde{\varphi}_{[k2]} = \exp\left[i\tilde{\boldsymbol{\chi}}_{[k2]}\left(x + \tfrac{1}{2}\tilde{\boldsymbol{\chi}}_{[k2]}t\right)\right]. \tag{A19}$$

Figures 7 and 8 show the amplitudes of the solutions in the cases $N = 2$ and 4 with the selected eigenvalues.

APPENDIX B: ORDINARY VECTOR SOLITON SOLUTIONS

Here we present the vector soliton solutions constructed by a Darboux transformation. Two cases are considered: (i) $a_1 = a_2 = 0$ and (ii) $a_1 \neq 0$ and $a_2 = 0$.

1. Nondegenerate bright solitons with $a_1 = a_2 = 0$

When $a_1 = a_2 = 0$, we have, from Eq. (10),

$$\lambda_{[1]} = \boldsymbol{\chi}_{[1]}. \tag{B1}$$

The eigenvalue $\boldsymbol{\chi}_{[1]}$ is given by Eq. (50). However, as mentioned above, we must have $\boldsymbol{\chi}_{[1]} = \boldsymbol{\chi}_2$ or $\boldsymbol{\chi}_3$. Using such an eigenvalue (or spectral parameter) and solving the associated Lax pair with zero seed solution, we have the eigenfunctions $\Phi_{[1]} = (R_{[1]}, S_{[1]}, W_{[1]})$,

$$R_{[1]} = \exp\left[i\boldsymbol{\chi}_{[1]}\left(x + \tfrac{1}{2}\boldsymbol{\chi}_{[1]}t\right)\right],$$
$$S_{[1]} = C_{s[1]},$$
$$W_{[1]} = C_{w[1]}. \tag{B2}$$

Here $C_{s[1]}$ and $C_{w[1]}$ are real constants. Performing the Darboux transformation (A10) with $\psi_0^{(j)} = 0$, we obtain the fundamental vector bright soliton solution. The higher-order iterations of the Darboux transformation lead to the nondegenerate soliton shown in Sec. VII A. The Nth-order soliton solution can be written as

$$\psi_N^{(1)} = -(\lambda_{[N]}^* - \lambda_{[N]}) \sum_{i=1}^{N-1} \mathbf{P}_{12}^{[N]}, \tag{B3}$$

$$\psi_N^{(2)} = -(\lambda_{[N]}^* - \lambda_{[N]}) \sum_{i=1}^{N-1} \mathbf{P}_{13}^{[N]}, \tag{B4}$$

where

$$\mathbf{T}^{[N]} = \mathbf{I} - \frac{\lambda_{[N]} - \lambda_{[N]}^*}{\lambda - \lambda_{[N]}^*} \mathbf{P}^{[N]}, \tag{B5}$$

$$\mathbf{P}^{[N]} = \frac{\Phi_{[N]}^{[N-1]} \Phi_{[N]}^{[N-1]\dagger}}{\Phi_{[N]}^{[N-1]\dagger} \Phi_{[N]}^{[N-1]}}, \tag{B6}$$

$$\Phi_{[N]}^{[N-1]} = (\mathbf{T}^{[N-1]}\mathbf{T}^{[N-2]} \cdots \mathbf{T}^{[1]}\mathbf{T}^{[0]})|_{\lambda=\lambda_{[N]}} \Phi_{[N]}. \tag{B7}$$

Here $\mathbf{T}^{[0]} = \mathbf{I}$ is the identity matrix. The eigenfunctions $\Phi_{[N]} = (R_{[N]}, S_{[N]}, W_{[N]})$ corresponding to N different spectral parameters $\lambda_{[1]}, \lambda_{[2]}, \ldots, \lambda_{[N]}$ are given by

$$R_{[N]} = \exp\left[i\boldsymbol{\chi}_{[N]}\left(x + \tfrac{1}{2}\boldsymbol{\chi}_{[N]}t\right)\right],$$
$$S_{[N]} = C_{s[N]},$$
$$W_{[N]} = C_{w[N]}. \tag{B8}$$

Letting $C_{s[1]} = C_{w[2]} = 1$ and $C_{w[1]} = C_{s[2]} = 0$, we obtain the nondegenerate soliton solution (51) with $N = 2$. The profiles are shown in Fig. 11. Furthermore, the fourth-order soliton solutions with $C_{s[3]} = C_{w[4]} = 1$ and $C_{w[3]} = C_{s[4]} = 0$ describe the interaction between two nondegenerate solitons shown in Fig. 12.

2. Nondegenerate localized waves with $a_1 \neq 0$ and $a_2 = 0$

In this case, we have, from Eq. (10),

$$\lambda_{[1]} = \chi_{[1]} - \frac{a_1^2}{\chi_{[1]} + \beta_1}. \tag{B9}$$

The eigenvalue $\chi_{[1]}$ is given by Eq. (53). However, as mentioned above, we must have $\chi_{[1]} = \chi_1(\chi_3)$ or χ_2. Here we first consider the eigenvalue $\chi_{[1]} = \chi_1$. The corresponding eigenfunctions $(R_{[1]}, S_{[1]}, W_{[1]})$ are given by

$$R_{[1]} = \varphi_{[1]} + \tilde{\varphi}_{[1]}, \tag{B10}$$

$$S_{[1]} = \psi_0^{(1)} \left(\frac{\varphi_{[1]}}{\beta_1 + \chi_{[1]}} + \frac{\tilde{\varphi}_{[1]}}{\beta_1 + \tilde{\chi}_{[1]}} \right), \tag{B11}$$

$$W_{[1]} = 0, \tag{B12}$$

where $\tilde{\chi}_{[1]} = \chi_{[1]} + i\alpha$ and

$$\varphi_{[1]} = \exp\left[i\chi_{[1]}\left(x + \tfrac{1}{2}\chi_{[1]}t\right)\right], \tag{B13}$$

$$\tilde{\varphi}_{[1]} = \exp\left[i\tilde{\chi}_{[1]}\left(x + \tfrac{1}{2}\tilde{\chi}_{[1]}t\right)\right]. \tag{B14}$$

The first-order solution obtained through the Darboux transformation is

$$\psi_1^{(1)} = \psi_0^{(1)} + \frac{(\lambda_{[1]}^* - \lambda_{[1]})R_{[1]}^* S_{[1]}}{|R_{[1]}|^2 + |S_{[1]}|^2 + |W_{[1]}|^2}, \tag{B15}$$

$$\psi_1^{(2)} = 0. \tag{B16}$$

The solution (B15) contains a KMS but only in the $\psi_1^{(1)}$ component.

To obtain the nondegenerate localized waves shown in Sec. VII B, we apply the second step of the Darboux

transformation. Note that the second spectral parameter used here is different from that in the first step, namely, $\lambda_{[2]} = \chi_{[2]} - \frac{a_1^2}{\chi_{[2]} + \beta_1}$, where $\chi_{[2]} = \chi_2$. The corresponding eigenvalues are given by

$$R_{[2]} = \exp\left[i\chi_{[2]}\left(x + \tfrac{1}{2}\chi_{[2]}t\right)\right], \tag{B17}$$

$$S_{[2]} = \psi_0^{(1)} \left(\frac{\exp[i\chi_{[2]}(x + \tfrac{1}{2}\chi_{[2]}t)]}{\beta_1 + \chi_{[2]}} \right), \tag{B18}$$

$$W_{[2]} = \exp(i\theta_2) \left(\frac{\exp[i\chi_{[2]}(x + \tfrac{1}{2}\chi_{[2]}t)]}{\beta_2 + \chi_{[2]}} \right). \tag{B19}$$

Finally, the second-order solution which describes the nondegenerate localized waves shown in Fig. 13 can be written as

$$\begin{aligned} \psi_2^{(1)} &= \psi_1^{(1)} + \frac{2i(\lambda_{[2]}^* - \lambda_{[2]})\Phi_1^* \Phi_2}{|\Phi_1|^2 + |\Phi_2|^2 + |\Phi_3|^2}, \\ \psi_2^{(2)} &= \frac{2i(\lambda_{[2]}^* - \lambda_{[2]})\Phi_1^* \Phi_3}{|\Phi_1|^2 + |\Phi_2|^2 + |\Phi_3|^2}, \end{aligned} \tag{B20}$$

where

$$\Phi_1 = \Delta \left[\left(\frac{1}{\Delta} + \frac{R_{[1]}R_{[1]}^*}{\phi^2} \right) R_{[2]} + \frac{R_{[1]}S_{[1]}^*}{\phi^2} S_{[2]} \right], \tag{B21}$$

$$\Phi_2 = \Delta \left[\frac{S_{[1]}R_{[1]}^*}{\phi^2} R_{[2]} + \left(\frac{1}{\Delta} + \frac{S_{[1]}S_{[1]}^*}{\phi^2} \right) S_{[2]} \right], \tag{B22}$$

$$\Phi_3 = W_{[2]}. \tag{B23}$$

Here $\Delta = \frac{\lambda_{[1]}^* - \lambda_{[1]}}{\lambda_{[2]} - \lambda_{[1]}^*}$ and $|\phi|^2 = |R_{[1]}|^2 + |S_{[1]}|^2$.

---

[1] N. Akhmediev and A. Ankiewicz, *Solitons: Nonlinear Pulses and Beams* (Chapman and Hall, London, 1997).

[2] N. Akhmediev and A. Ankiewicz, in *Dissipative Solitons*, edited by N. Akhmediev and A. Ankiewicz, Lecture Notes in Physics Vol. 661 (Springer, Berlin, 2005).

[3] N. Akhmediev and A. Ankiewicz, *Dissipative Solitons: From Optics to Biology and Medicine* (Springer, Berlin, 2008).

[4] S. Flach and A. V. Gorbach, Discrete breathers—Advances in theory and applications, Phys. Rep. **467**, 1 (2008).

[5] F. Lederer, G. I. Stegeman, D. N. Christodoulides, G. Assanto, M. Segev, and Y. Silberberg, Discrete solitons in optics, Phys. Rep. **463**, 1 (2008).

[6] Y. V. Kartashov, B. A. Malomed, and L. Torner, Solitons in nonlinear lattices, Rev. Mod. Phys. **83**, 247 (2011).

[7] V. V. Konotop, J. Yang, and D. A. Zezyulin, Nonlinear waves in $\mathcal{PT}$-symmetric systems, Rev. Mod. Phys. **88**, 035002 (2016).

[8] J. M. Dudley, F. Dias, M. Erkintalo, and G. Genty, Instabilities, breathers and rogue waves in optics, Nat. Photon. **8**, 755 (2014).

[9] J. M. Dudley, G. Genty, A. Mussot, A. Chabchoub, and F. Dias, Rogue waves and analogies in optics and oceanography, Nat. Rev. Phys. **1**, 675 (2019).

[10] M. Sato, B. E. Hubbard, and A. J. Sievers, Colloquium: Nonlinear energy localization and its manipulation in micromechanical oscillator arrays, Rev. Mod. Phys. **78**, 137 (2006).

[11] H. Xiong, J. Gan, and Y. Wu, Kuznetsov-Ma Soliton Dynamics Based on the Mechanical Effect of Light, Phys. Rev. Lett. **119**, 153901 (2017).

[12] N. Akhmediev and V. I. Korneev, Modulation instability and periodic solutions of the nonlinear Schrödinger equation, Theor. Math. Phys. **69**, 1089 (1986).

[13] C. Liu, Y.-H. Wu, S.-C. Chen, X. Yao, and N. Akhmediev, Exact Analytic Spectra of Asymmetric Modulation Instability in Systems with Self-Steepening Effect, Phys. Rev. Lett. **127**, 094102 (2021).

[14] N. Akhmediev, *Déjà vu* in optics, Nature (London) **413**, 267 (2001).

[15] N. Akhmediev, A. Ankiewicz, and J. M. Soto-Crespo, in *Nonlinear Guided Wave Optics: A Testbed for Extreme Waves*, edited by S. Wabnitz (IOP, Bristol, 2017).

[16] J. M. Dudley, G. Genty, and S. Coen, Supercontinuum generation in photonic crystal fiber, Rev. Mod. Phys. **78**, 1135 (2006).

[17] J. M. Soto-Crespo, N. Devine, and N. Akhmediev, Intergrable Turbulence and Rogue Waves: Breathers or Solitons? Phys. Rev. Lett. **116**, 103901 (2016).

[18] N. Akhmediev, V. M. Eleonskii, and N. E. Kulagin, Exact first-order solutions of the nonlinear Schrödinger equation, Theor. Math. Phys. **72**, 809 (1987).

[19] M. Conforti, A. Mussot, A. Kudlinski, S. Trillo, and N. Akhmediev, Doubly periodic solutions of the focusing nonlinear Schrödinger equation: Recurrence, period doubling, and amplification outside the conventional modulation-instability band, Phys. Rev. A **101**, 023843 (2020).

[20] E. A. Kuznetsov, Solitons in a parametrically unstable plasma, Sov. Phys. Dokl. **22**, 575 (1977).

[21] Y. C. Ma, The Perturbed plane wave solutions of the cubic nonlinear Schrödinger equation, Stud. Appl. Math. **60**, 43 (1979).

[22] M. Bertola and A. Tovbis, Universality for the Focusing nonlinear schrödinger equation at the gradient catastrophe point: rational breathers and poles of the tritronquée solution to painlevé I, Commun. Pure Appl. Math. **66**, 678 (2013).

[23] A. Tikan, C. Billet, G. El, A. Tovbis, M. Bertola, T. Sylvestre, F. Gustave, S. Randoux, G. Genty, P. Suret, and J. M. Dudley, Universality of the Peregrine Soliton in the Focusing Dynamics of the Cubic Nonlinear Schrodinger Equation, Phys. Rev. Lett. **119**, 033901 (2017).

[24] N. Akhmediev and S. Wabnitz, Phase detecting of solitons by mixing with a continuous-wave background in an optical fiber, J. Opt. Soc. Am. B **9**, 236 (1992).

[25] L.-C. Zhao, L. Ling, and Z.-Y. Yang, Mechanism of Kuznetsov-Ma breathers, Phys. Rev. E **97**, 022218 (2018).

[26] B. Kibler, J. Fatome, C. Finot, G. Millot, G. Genty, B. Wetzel, N. Akhmediev, F. Dias, and J. M. Dudley, Observation of Kuznetsov-Ma soliton dynamics in optical fibre, Sci. Rep. **2**, 463 (2012).

[27] A. Chabchoub, B. Kibler, J. M. Dudley, and N. Akhmediev, Hydrodynamics of periodic breathers, Philos. Trans. R. Soc. A **372**, 20140005 (2014).

[28] E. Lucas, M. Karpov, H. Guo, M. L. Gorodetsky, and T. J. Kippenberg, Breathing dissipative solitons in optical microresonators, Nat. Commun. **8**, 736 (2017).

[29] J. Peng, S. Boscolo, Z. Zhao, and H. Zeng, Breathing dissipative solitons in mode-locked fiber lasers, Sci. Adv. **5**, 1110 (2019).

[30] J. Satsuma and N. Yajima, Initial value problems of one-dimensional self-modulation of nonlinear waves in dispersive media, Prog. Theor. Phys. Suppl. **55**, 284 (1974).

[31] L. F. Mollenauer, R. H. Stolen, and J. P. Gordon, Experimental Observation of Picosecond Pulse Narrowing and Solitons in Optical Fibers, Phys. Rev. Lett. **45**, 1095 (1980).

[32] A. Chabchoub, N. Hoffmann, M. Onorato, G. Genty, J. M. Dudley, and N. Akhmediev, Hydrodynamic Supercontinuum, Phys. Rev. Lett. **111**, 054104 (2013).

[33] G. Agrawal, *Nonlinear Fiber Optics*, 5th ed. (Academic, San Diego, 2012)

[34] P. G. Kevrekidis, D. Frantzeskakis, and R. Carretero-Gonzalez, *Emergent Nonlinear Phenomena in Bose-Einstein Condensates: Theory and Experiment* (Springer, Berlin, 2009)

[35] M. Onorato, A. R. Osborne, and M. Serio, Modulational Instability in Crossing Sea States: A Possible Mechanism for the Formation of Freak Waves, Phys. Rev. Lett. **96**, 014503 (2006).

[36] A. Degasperis and S. Lombardo, in *Rogue and Shock Waves in Nonlinear Dispersive Media*, Lecture Notes in Physics Vol. 926, edited by M. Onorato, S. Residori, and F. Baronio (Springer, New York, 2016).

[37] B. L. Guo and L. M. Ling, Rogue wave, breathers and bright-dark-rogue solutions for the coupled Schrödinger equations, Chin. Phys. Lett. **28**, 110202 (2011).

[38] C. Kalla, Breathers and solitons of generalized nonlinear Schrödinger equations as degenerations of algebro-geometric solutions, J. Phys. A: Math. Theor. **44**, 335210 (2011).

[39] F. Baronio, A. Degasperis, M. Conforti, and S. Wabnitz, Solutions of the Vector Nonlinear Schrödinger Equations: Evidence for Deterministic Rogue Waves, Phys. Rev. Lett. **109**, 044102 (2012).

[40] L.-C. Zhao and J. Liu, Localised nonlinear waves in a two-mode nonlinear fiber, J. Opt. Soc. Am. B **29**, 3119 (2012).

[41] L.-C. Zhao and J. Liu, Rogue-wave solutions of a three-component coupled nonlinear Schrödinger equation, Phys. Rev. E **87**, 013201 (2013).

[42] A. Degasperis and S. Lombardo, Rational solitons of wave resonant-interaction models, Phys. Rev. E **88**, 052914 (2013).

[43] F. Baronio, M. Conforti, A. Degasperis, S. Lombardo, M. Onorato, and S. Wabnitz, Vector Rogue Waves and Baseband Modulation Instability in the Defocusing Regime, Phys. Rev. Lett. **113**, 034101 (2014).

[44] C. Liu, Z.-Y. Yang, L.-C. Zhao, and W.-L Yang, Vector breathers and the inelastic interaction in a three-mode nonlinear optical fiber, Phys. Rev. A **89**, 055803 (2014).

[45] S. Chen, F. Baronio, J. M. Soto-Crespo, P. Grelu, and, D. Mihalache, Versatile rogue waves in scalar, vector, and multi-dimensional nonlinear systems, J. Phys. A: Math. Theor. **50**, 463001 (2017).

[46] L. Ling and L.-C. Zhao, Modulational instability and homoclinic orbit solutions in vector nonlinear Schrödinger equation, Commun. Nonlinear Sci. Num. Simulat. **72**, 449 (2019).

[47] S.-C. Chen, C. Liu, X. Yao, L.-C. Zhao, and N. Akhmediev, Extreme spectral asymmetry of Akhmediev breathers and Fermi-Pasta-Ulam recurrence in a Manakov system, Phys. Rev. E **104**, 024215 (2021).

[48] B. Frisquet, B. Kibler, P. Morin, F. Baronio, M. Conforti, G. Millot, and S. Wabnitz, Optical dark rogue waves, Sci. Rep. **6**, 20785 (2016).

[49] F. Baronio, B. Frisquet, S. Chen, G. Millot, S. Wabnitz, and B. Kibler, Observation of a group of dark rogue waves in a telecommunication optical fiber, Phys. Rev. A **97**, 013852 (2018).

[50] S. Stalin, R. Ramakrishnan, M. Senthilvelan, and M. Lakshmanan, Nondegenerate Solitons in Manakov System, Phys. Rev. Lett. **122**, 043901 (2019).

[51] Y.-H. Qin, L.-C. Zhao, and L. M. Ling, Nondegenerate bound-state solitons in multicomponent Bose-Einstein condensates, Phys. Rev. E **100**, 022212 (2019).

[52] R. Ramakrishnan, S. Stalin, and M. Lakshmanan, Nondegenerate solitons and their collisions in Manakov systems, Phys. Rev. E **102**, 042212 (2020).

[53] Y.-H. Qin, L.-C. Zhao, Z.-Q. Yang, and L. Ling, Multivalley dark solitons in multicomponent Bose-Einstein condensates with repulsive interactions, Phys. Rev. E **104**, 014201 (2021).

[54] S. V. Manakov, On the theory of two-dimensional stationary self-focusing of electromagnetic waves, Sov. Phys. JETP **38**, 248 (1974).

[55] N. V. Priya, M. Senthilvelan, and M. Lakshmanan, Akhmediev breathers, Ma solitons, and general breathers from rogue waves: A case study in the Manakov system, Phys. Rev. E **88**, 022918 (2013).

[56] K. Hammani, B. Wetzel, B. Kibler, J. Fatome, C. Finot, G. Millot, N. Akhmediev, and J. M. Dudley, Spectral dynamics

of modulation instability described using Akhmediev breather theory, Opt. Lett. **36**, 2140 (2011).

[57] N. Akhmediev and A. Ankiewicz, Partially Coherent Solitons on a Finite Background, Phys. Rev. Lett. **82**, 2661 (1999).

[58] N. Akhmediev and A. Ankiewicz, Multi-soliton complexes, Chaos **10**, 600 (2000).

[59] Q.-H. Park and H. J. Shin, Systematic construction of multi-component optical solitons, Phys. Rev. E **61**, 3093 (2000).

[60] E. G. Charalampidis, W. Wang, P. G. Kevrekidis, D. J. Frantzeskakis, and J. Cuevas-Maraver, SO(2)-induced breathing patterns in multicomponent Bose-Einstein condensates, Phys. Rev. A **93**, 063623 (2016).

[61] L.-C. Zhao, Beating effects of vector solitons in Bose-Einstein condensates, Phys. Rev. E **97**, 062201 (2018).

[62] D. J. Kedziora, A. Ankiewicz, and N. Akhmediev, Second-order nonlinear Schrodinger equation breather solutions in the degenerate and rogue wave limits, Phys. Rev. E **85**, 066601 (2012).

[63] G. A. El, A. V. Gurevich, V. V. Khodorovskii, and A. L. Krylov, Modulational instability and formation of a nonlinear oscillatory structure in a focusing medium, Phys. Lett. A **177**, 357 (1993).

[64] G. Biondini and D. Mantzavinos, Universal Nature of the Nonlinear Stage of Modulational Instability, Phys. Rev. Lett. **116**, 043902 (2016).

[65] A. E. Kraych, P. Suret, G. El, and S. Randoux, Nonlinear Evolution of the Locally Induced Modulational Instability in Fiber Optics, Phys. Rev. Lett. **122**, 054101 (2019).

[66] M. Conforti, S. Li, G. Biondini, and S. Trillo, Auto-modulation versus breathers in the nonlinear stage of modulational instability, Opt. Lett. **43**, 5291 (2018).